Line plus arc source trajectories and their R-line coverage for long-object cone-beam imaging with a C-arm system

2011 Phys. Med. Biol. 56 3447

(http://iopscience.iop.org/0031-9155/56/12/001)

IOP PUBLISHING PHYSICS IN MEDICINE AND BIOLOGY

Phys. Med. Biol. **56** (2011) 3447–3471 doi:10.1088/0031-9155/56/12/001

Line plus arc source trajectories and their R-line coverage for long-object cone-beam imaging with a C-arm system

Zhicong Yu[1], Adam Wunderlich[1], Frank Dennerlein[2], Günter Lauritsch[2] and Frédéric Noo[1]

[1] Department of Radiology, University of Utah, Salt Lake City, UT, USA
[2] Siemens AG, Healthcare Sector, Forchheim, Germany

E-mail: zyu@ucair.med.utah.edu, awunder@ucair.med.utah.edu and noo@ucair.med.utah.edu

Received 4 October 2010, in final form 17 April 2011
Published 23 May 2011
Online at stacks.iop.org/PMB/56/3447

Abstract

Cone-beam imaging with C-arm systems has become a valuable tool in interventional radiology. Currently, a simple circular trajectory is used, but future applications should use more sophisticated source trajectories, not only to avoid cone-beam artifacts but also to allow extended volume imaging. One attractive strategy to achieve these two goals is to use a source trajectory that consists of two parallel circular arcs connected by a line segment, possibly with repetition. In this work, we address the question of R-line coverage for such a trajectory. More specifically, we examine to what extent R-lines for such a trajectory cover a central cylindrical region of interest (ROI). An R-line is a line segment connecting any two points on the source trajectory. Knowledge of R-line coverage is crucial because a general theory for theoretically exact and stable image reconstruction from axially truncated data is only known for the points in the scanned object that lie on R-lines. Our analysis starts by examining the R-line coverage for the elemental trajectories consisting of (i) two parallel circular arcs and (ii) a circular arc connected orthogonally to a line segment. Next, we utilize our understanding of the R-lines for the aforementioned elemental trajectories to determine the R-line coverage for the trajectory consisting of two parallel circular arcs connected by a tightly fit line segment. For this trajectory, we find that the R-line coverage is insufficient to completely cover any central ROI. Because extension of the line segment beyond the circular arcs helps to increase the R-line coverage, we subsequently propose a trajectory composed of two parallel circular arcs connected by an extended line. We show that the R-lines for this trajectory can fully cover a central ROI if the line extension is long enough. Our presentation includes a formula for the minimum line extension needed to achieve full R-line coverage of an ROI with a specified size, and also includes a preliminary study on the

required detector size, showing that the R-lines added by the line extension are not constraining.

(Some figures in this article are in colour only in the electronic version)

1. Introduction

Over the last decade, cone-beam (CB) computed tomography (CT) has become a valuable tool in interventional radiology. Its success stems from its ability to provide the physician with immediate feedback during a clinical procedure, thereby allowing on-the-fly adjustments. So far, circular data acquisition has been used, but more sophisticated geometries are being considered due to the problem of CB artifacts and also due to limited volume coverage.

An attractive source trajectory for extended volume imaging with no CB artifacts is the helix. This trajectory has been very successful in diagnostic CT, but it is unfortunately not practical for interventional radiology. The problem is the need for a slip-ring technology, which is difficult to implement (at reasonable cost) on C-arm systems. To perform extended volume imaging with a C-arm system, another geometry must be found. Many options are possible, from using a combination of circles and lines (or arcs) (Katsevich 2004a, 2005, Hoppe *et al* 2006) to using a reverse helix, as suggested by the group of X Pan at the University of Chicago (Cho *et al* 2008). The reverse helix has many merits, but efficient and accurate reconstruction from axially truncated data collected on such a helix appears to be challenging (Cho *et al* 2008, 2010, Noo *et al* 2009). The main difficulty stems from the fact that the R-lines do not cover the whole scanned object (an R-line is any line segment that connects two source positions). More specifically, the reverse helix is such that the theories that have been found for efficient handling of axial truncation (Katsevich 2004b, Zou and Pan 2004, Pack *et al* 2005, Pack and Noo 2005, Ye *et al* 2005) cannot be applied, because large portions of the object are not intersected by R-lines.

In this work, we revisit the option of performing extended field-of-view imaging using a sequence of circular short-scans connected by line segments. In particular, we investigate R-line coverage with the goal of finding source-trajectory parameters such that a central cylindrical region-of-interest (ROI) within the object is fully covered by R-lines.

The paper is organized as follows. First, we describe the source trajectory of interest. Next, we discuss the R-line coverage resulting from two parallel circular arcs and also the R-line coverage resulting from connecting a line orthogonally to the endpoint of a circular arc. Subsequently, we are able to present the R-line coverage for the entire source trajectory. Our analysis shows that R-line coverage is inadequate when the line scans have their endpoints on the arcs. On the other hand, when the line scans are allowed to extend beyond the arcs, we find that the full coverage of a central cylindrical ROI becomes possible. The required line extension is analyzed as a function of the ROI radius and the length of the circular arcs, and a preliminary analysis on detector size requirement is given.

2. Source-trajectory geometries

In this section, we introduce two source trajectories composed of circular arcs and a line segment. Then, we introduce the terminology that is used in this work as well as a geometrical theorem that will be needed later.

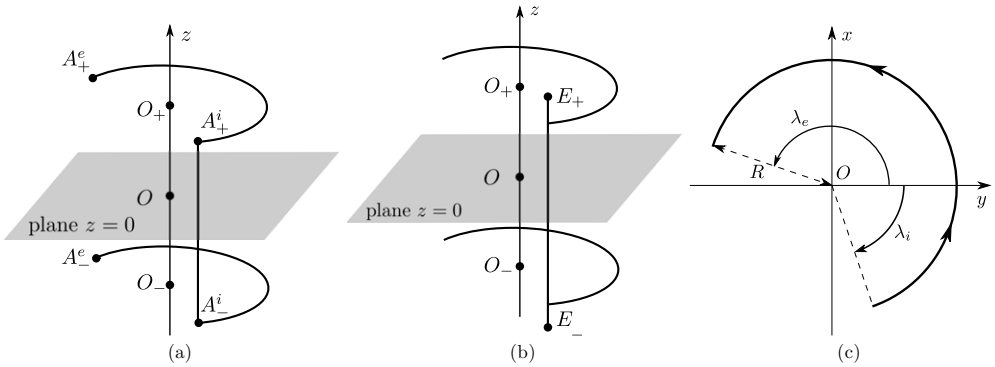

Figure 1. Source-trajectory geometries. Extended volume imaging is performed using duplicates of a path consisting of two circular arcs plus a line. Two options are considered for this path: (a) the line is tightly fit between the arcs, so that each endpoint of the line corresponds to one endpoint of an arc, and (b) the line extends beyond the arcs by a distance Δh on each side. Figure (c) shows the orthogonal projection of the source trajectory onto the x–y plane. Points $O_- = (0, 0, -H)$ and $O_+ = (0, 0, H)$ are the centers of the lower and upper arcs, respectively. Points $E_- = (R\cos\lambda_i, R\sin\lambda_i, -H - \Delta h)$ and $E_+ = (R\cos\lambda_i, R\sin\lambda_i, H + \Delta h)$ are the extremities of the extended line. The polar angles λ_i and λ_e define the initial and end points of each arc.

2.1. Source trajectories

We consider extended volume imaging using periodic duplicates of a source trajectory consisting of two circular arcs connected by a line segment. The patient is assumed to lie along the z-axis, the arcs are in parallel planes that are orthogonal to this axis, and the line is orthogonal to each arc through one of its endpoints. Figure 1 depicts this trajectory. Two options are considered: (a) the line is spatially limited by the arcs and (b) the line extends beyond the arcs. In the first option, the trajectory is called the arc–line–arc (ALA) trajectory; in the second option, it is called the arc–extended-line–arc (AELA) trajectory. Figure 1 also shows how each circular arc is oriented relative to the x- and y-axes that form together with the z-axis a Cartesian system of coordinates. The distance in z between the arcs is $2H$, the radius of the arcs is R, and the line extension in option (b) is Δh on each end. Also, the plane $z = 0$ is chosen to be at mid-distance between the two arcs.

Throughout the text, the circular arcs and the line segment that together form the source trajectory are referred to as the T-arcs and the T-line, respectively, where T stands for *trajectory*. The T-arcs at $z = H$ and $z = -H$ are distinguished from each other using the terms upper and lower T-arcs, respectively. By extension, the term T-arc is also used to denote the orthogonal projection of either the upper or the lower T-arc onto any plane that is parallel to the x–y plane. The T-arc terminology is especially useful as it avoids confusion with other arcs that will appear later.

Note that the endpoints of the upper T-arc are denoted as A^i_+ and A^e_+, whereas the endpoints of the lower T-arc are A^i_- and A^e_-. By convention, the superscript i refers to the start (initial) point on the T-arc and the superscript e to the end point. The line segment is defined to pass through A^i_+ and A^i_-. The polar angle position of A^i_+ and A^i_- is denoted as λ_i, whereas the polar angle position of A^e_+ and A^e_- is denoted as λ_e.

By Tuy's condition (Tuy 1983), theoretically exact and stable reconstruction of the x-ray linear attenuation coefficient from CB projections is only possible within the convex hull of

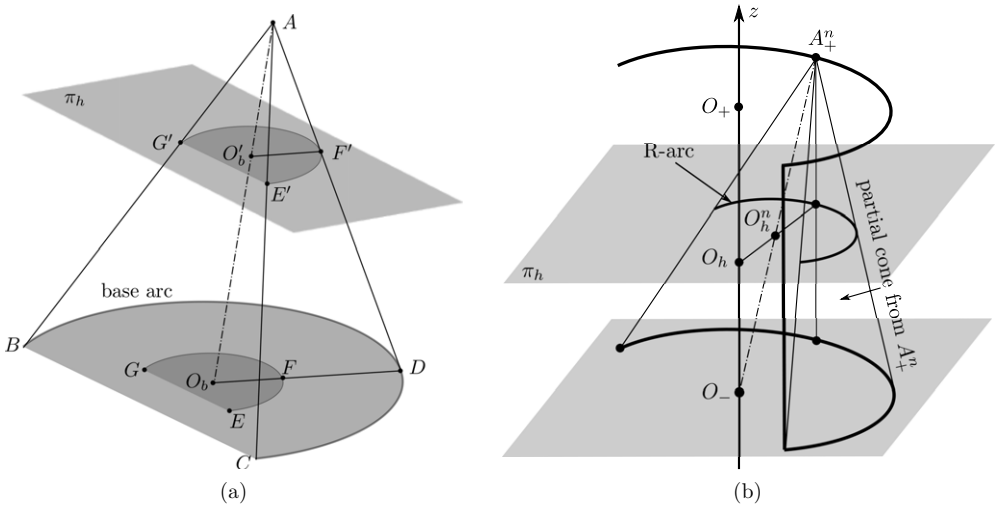

Figure 2. (a) Illustration of theorem 1. The plane π_h is parallel to the base plane and intersects the partial cone from point A along $\mathrm{Arc}(O_b')$; this arc can be obtained by isotropically scaling the base arc into $\mathrm{Arc}(O_b)$, then translating the result from O_b to O_b'. (b) Illustration of the upside cone from A_+^n.

the source trajectory (Finch 1985). Hence, we do not investigate R-line coverage outside this convex hull. To be more precise, we only investigate R-line coverage within a specific cylinder centered on the z-axis where Tuy's condition is fulfilled. This cylinder extends from $z = -H$ to $z = H$ and has radius R_m determined by the angular length, $\lambda_m = \lambda_e - \lambda_i$, of the T-arcs according to the equation

$$R_m = R\sin((\lambda_m - \pi)/2)\,. \tag{1}$$

Basically, R_m is the radius of the largest central cylinder within the convex hull of the source trajectory.

2.2. Preliminaries

Below, we introduce some terminology used in this work. First, note that we will make extensive use of the conical surface that is defined by a point and a circular arc, called the base arc, that are not coplanar. To simplify the text, we loosely refer to such a surface as being a partial cone. In order to aid with the understanding of our terminology and for later developments, we give the following theorem on partial cones that is proven in appendix A.

Theorem 1. *As illustrated in figure 2(a), the intersection between a partial cone and a plane that is parallel to the base of the cone is an arc that is a translation of a scaled copy of the base arc, with the scaling being isotropically applied relative to the center of the base arc.*

As shown in figure 2(b), a partial cone may be obtained by selecting one point A_+^n on the upper T-arc and connecting it to all of the points on the lower T-arc. Such a partial cone is called the upside cone from A_+^n. Similarly, a partial cone may be obtained by connecting any point on the lower T-arc to all of the points on the upper T-arc; such a partial cone is called a downside cone.

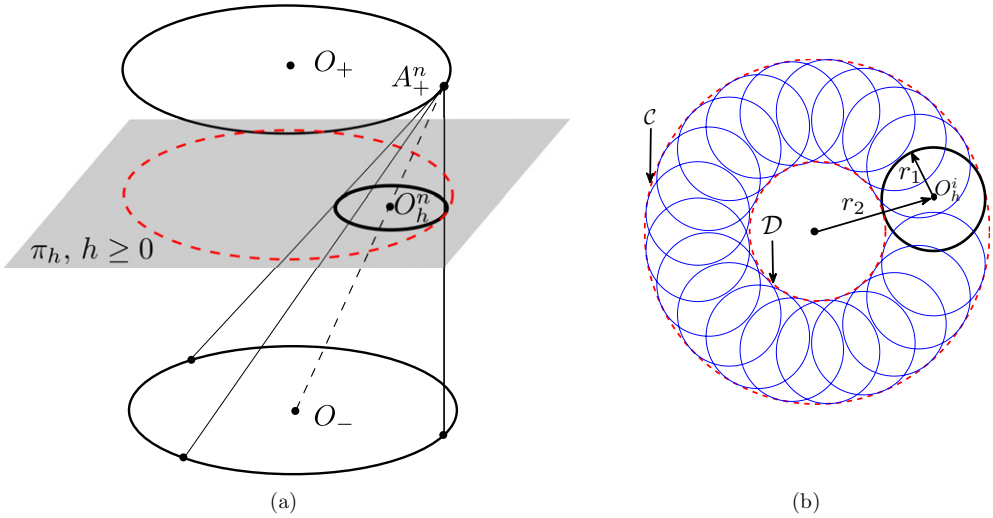

Figure 3. Arc–arc R-line coverage when the length of the T-arcs is 360°. (a) Coverage in the plane π_h due to one point from the upper T-arc; this coverage is a circle centered on a point denoted as O_h^n in the figure. (b) Coverage in the same plane as on the left, but due to several points on the upper T-arc.

Let π_h be the plane $z = h$, as illustrated in figure 2(b). Theorem 1 indicates that the intersection between π_h and any upside or downside cone is a circular arc. Throughout the paper, such an arc is called an R-arc, since it consists of points covered by R-lines. Furthermore, theorem 1 implies that the angular length of any R-arc is the same as the angular length of the T-arcs, and it also implies that the line connecting the endpoints of any R-arc is parallel to the line connecting the endpoints of either T-arc.

Two more interesting properties of R-arcs need to be noted. First, by construction, an R-arc is within the disk delimited by the T-arc inside π_h. Second, an R-arc always shares one (and only one) point with the T-arc; this point is the intersection of π_h with the line parallel to the z-axis through the vertex of the partial cone defining the R-arc. Consequently, every R-arc is tangent to the T-arc. See figures 3 and 4.

If an arc can be unambiguously identified by its center, we will denote it with the label of its center point; for example, we denote the lower T-arc in figure 2(b) as $\mathrm{Arc}(O_-)$ and the R-arc in figure 4(a) as $\mathrm{Arc}\left(O_h^i\right)$. Similarly, a circle that is unambiguously identifiable by its center, O, is referred to as $\mathrm{Cir}(O)$.

3. The ALA trajectory

In this section, we discuss the R-line coverage for the ALA trajectory. First, we examine the R-line coverage that is generated by connecting points from one T-arc to the other. Next, we consider the additional R-line coverage that results from connecting points on the T-line to points on the T-arcs. Note that the geometry of the problem at hand is mirror symmetric relative to the $z = 0$ plane. Therefore, the R-line coverage in the plane $z = z_0$ is the same as that in the plane $z = -z_0$ for any $0 \leqslant z_0 \leqslant H$. Hence, we only discuss the R-line coverage at positions $z \geqslant 0$.

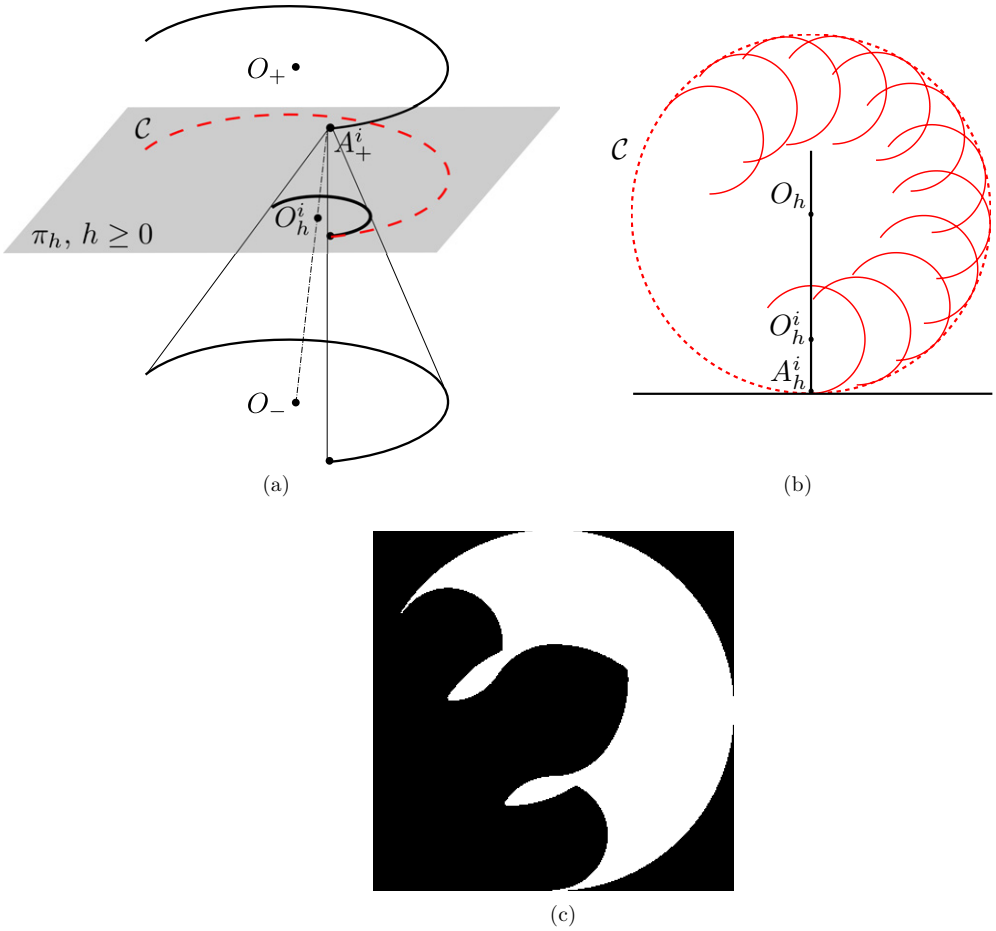

Figure 4. Arc–arc R-line coverage when the length of the T-arcs is 234°. (a) Coverage in π_h due to one point from the upper T-arc; this coverage is an R-arc centered on a point denoted as O_h^i in the figure. (b) Coverage in the same plane as in (a), but due to several points on the upper T-arc. (c) Full R-line coverage in π_h, as obtained using a numerical simulation.

3.1. Arc–arc coverage

To understand the R-line coverage for the elemental arc–arc (AA) trajectory, we start by considering the simpler case where each T-arc has a length of 360°. We choose a value for $h \in [0, H]$, draw π_h, and then find the R-line coverage within this plane. The situation is depicted in figure 3. Basically, we take a point on the upper T-arc, called A_+^n, and connect it to all points on the lower T-arc as shown in figure 3(a). Doing so, we create (the surface of) a cone that intersects π_h along a circle, called an R-circle (in analogy with the earlier-defined notion of an R-arc). This circle defines the R-line coverage coming from A_+^n in π_h. By continuously moving A_+^n along the upper T-arc, we obtain an infinite number of additional R-circles, a coarse sampling of which is shown in figure 3(b). The union of all the R-circles is the full R-line coverage in π_h. This union is an annular region with external boundary $\mathcal{C}$ and internal boundary $\mathcal{D}$ shown in figure 3(b). The boundary $\mathcal{C}$ is the T-arc in π_h.

As illustrated in figure 3(b), the R-line coverage within π_h is conveniently described by two parameters r_1 and r_2: r_1 is the radius of the R-circle, and r_2 is the radius of the circle formed by the union of the centers of the R-circles. By construction, both r_1 and r_2 are functions of h, and are easily found to be

$$r_1 = \frac{H-h}{2H}R \qquad \text{and} \qquad r_2 = R - r_1 = \frac{H+h}{2H}R. \tag{2}$$

Using the above formulae for r_1 and r_2, it follows that $\mathcal{D}$ has radius $r_{\mathcal{D}} = r_2 - r_1 = Rh/H$.

Now, we turn to the general situation where the T-arcs have an angular range of less than 360°. We again consider the R-line coverage in the plane π_h with $h \geqslant 0$, as illustrated in figure 4. Comparing figure 3(a) with figure 4(a), we see that the R-line coverage resulting from A_+^i is not an R-circle, it is an R-arc, albeit of the same radius, r_1. By moving A_+^i along the upper T-arc, we obtain a set of R-arcs whose union defines the R-line coverage within π_h, as shown in figure 4(b). Contrasting figure 3(b) with figure 4(b), we see that the R-line coverage for two T-arcs of angular length shorter than 360° is a subset of that for two 360° T-arcs. The R-line coverage resulting from a numerical simulation is shown in figure 4(c).

Note the following important property from figure 4(b): points O_h, O_h^i and A_h^i are aligned, where O_h is the center of the T-arc, O_h^i is the center of the R-arc, and A_h^i is the orthogonal projection of A_+^i onto π_h. This property is due to A_h^i being the point on the R-arc defined from A_+^i that is also on the T-arc. Indeed, under such circumstances, the line connecting O_h to A_h^i and the line connecting O_h^i to A_h^i both must be orthogonal to the tangent to the T-arc at A_h^i.

We now describe an efficient numerical procedure to identify the R-line coverage within any plane π_h. Afterward, we will give geometrical insight into the origin of the R-line coverage shown in figure 4(c). Efficient computation of the R-line coverage in π_h is made possible by the following corollary to theorem 1.

Corollary 1. *For the arc–arc trajectory, all of the R-arcs in the plane π_h are the translated versions of each other (with their radius being equal to r_1, as given by (2)).*

Proof. The corollary is a direct consequence of the following observations: (i) as discussed at the beginning of this section and illustrated with figure 3, all R-arcs in π_h have the same radius, namely r_1; (ii) by theorem 1, all R-arcs in π_h have the same angular length; and (iii) by theorem 1, all R-arcs in π_h are oriented in the same way as the T-arc, with the line connecting their endpoints being parallel to the line connecting the endpoints of the T-arc.

Analytically, the corollary can also be explained as follows. Consider two R-arcs in π_h. By definition, each of these two R-arcs comes from the intersection of an upside cone with π_h, so that, by theorem 1, any point $\vec{x}$ on the lower T-arc can be associated with a point $\vec{x}_1 = s_1\vec{x} + \vec{t}_1$ on the first R-arc and a point $\vec{x}_2 = s_2\vec{x} + \vec{t}_2$ on the second R-arc, with s_1 and s_2 being scaling constants and $\vec{t}_1$ and $\vec{t}_2$ being translation vectors, all independent of $\vec{x}$. Since all R-arcs in π_h have the same radius, we have $s_1 = s_2$ and thus $\vec{x}_2 = \vec{x}_1 + \vec{c}$ where $\vec{c} = \vec{t}_2 - \vec{t}_1$ is independent of $\vec{x}$. Hence, the two R-arcs are translations of each other. □

Let $\vec{e}_z$ be the unit vector pointing in the z-direction. Thanks to the corollary, any point $\vec{x} \in \pi_h$ that belongs to an R-line can be parameterized using two angles, λ and ϕ, according to

$$\vec{x} = r_2\big(\cos\lambda\,\vec{n}_i + \sin\lambda\,\vec{n}_i^{\perp}\big) + r_1\big(\cos\phi\,\vec{n}_i + \sin\phi\,\vec{n}_i^{\perp}\big) + h\,\vec{e}_z, \tag{3}$$

where $\vec{n}_i$ is the unit vector in π_h that goes from the center of the T-arc toward the initial point on the T-arc, and $\vec{n}_i^{\perp}$ is obtained by rotating $\vec{n}_i$ about the z-axis by 90° in the counter-clockwise direction. This equation may be best understood by looking at figure 5, where two R-arcs are shown in π_h: $\mathrm{Arc}\big(O_h^i\big)$ which starts at the initial point on the T-arc, A_h^i, and $\mathrm{Arc}\big(O_h^n\big)$ which is arbitrary, with its initial point denoted as A_h^n. By corollary 1, the line that connects O_h^n to

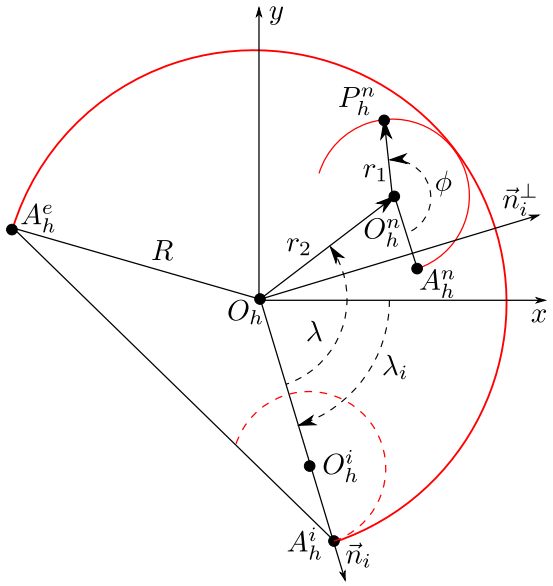

Figure 5. The R-line coverage in π_h can be fully parameterized with two angles, λ and ϕ, varying both over $[0, \lambda_m]$. Angle λ is used to specify the center of the *R*-arc, whereas angle ϕ is used to specify a location on the R-arc, which is identified as P_h^n in the figure. The meaning of the other symbols is as follows: R is the radius of the T-arc; r_1 is the radius of the R-arc; r_2 is the distance between the z-axis and the center of the R-arc; $\vec{n}_i$ is the unit vector pointing from the center O_h to the initial point A_h^i.

A_h^n is parallel to the line that passes through O_h, O_h^i and A_h^i, where O_h is the center of the T-arc in π_h. Vector $\vec{n}_i$ is the common direction of these two lines. The first term in (3) selects the position of the center of the arbitrary R-arc relative to the line of direction $\vec{n}_i$ through A_h^i, whereas the second term selects a point on the arbitrary R-arc, relative to the line of direction $\vec{n}_i$ through A_h^n. Naturally, angles λ and ϕ in (3) are not allowed to take arbitrary values; they are constrained to lie between 0 and λ_m.

An efficient algorithm for computation of the R-line coverage in π_h is obtained by inverting equation (3) to obtain λ and ϕ as functions of the first two coordinates of $\vec{x}$, denoted as x and y. First, note from figure 3 that for a given (x, y), there are at most two solutions, denoted (λ_+, ϕ_+) and (λ_-, ϕ_-), and these solutions only exist if $(r_1 - r_2)^2 \leqslant x^2 + y^2 \leqslant (r_1 + r_2)^2$. Since $\vec{n}_i = [\cos\lambda_i, \sin\lambda_i, 0]$, we have

$$\begin{cases} x = r_2\cos(\lambda + \lambda_i) + r_1\cos(\phi + \lambda_i) \\ y = r_2\sin(\lambda + \lambda_i) + r_1\sin(\phi + \lambda_i), \end{cases} \tag{4}$$

and thus

$$(x - r_2\cos(\lambda + \lambda_i))^2 + (y - r_2\sin(\lambda + \lambda_i))^2 = r_1^2\,. \tag{5}$$

Using ρ and θ for the polar coordinates of (x, y), (5) yields

$$\cos(\lambda + \lambda_i - \theta) = \frac{\rho^2 + r_2^2 - r_1^2}{2\rho r_2}\,, \tag{6}$$

which gives the following expressions for λ_+ and λ_-:

$$\lambda_+ = \mathrm{mod}(\theta - \lambda_i + \eta, 2\pi) \tag{7}$$

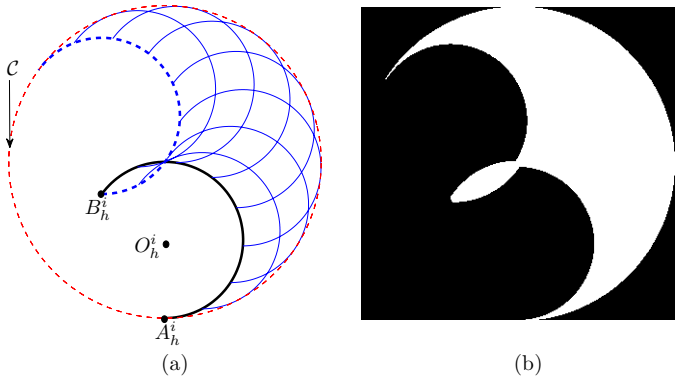

Figure 6. Arc–arc R-line coverage in the plane π_h when $h = 0$ and the length of the T-arcs is 234°. (a) R-line coverage of the AA trajectory due to several points on the upper T-arc. (b) Full R-line coverage in π_h, as obtained using numerical simulation.

$$\lambda_- = \mathrm{mod}(\theta - \lambda_i - \eta, 2\pi) \tag{8}$$

with $\mathrm{mod}(u, 2\pi)$ being equal to u modulo 2π, and with

$$\eta = \arccos\left(\frac{\rho^2 + r_2^2 - r_1^2}{2\rho r_2}\right), \tag{9}$$

which is a real number as long as $r_2 - r_1 \leqslant \rho \leqslant r_2 + r_1$. Rewriting (4) in the form

$$\begin{cases} r_1 \cos(\phi + \lambda_i) = x - r_2 \cos(\lambda + \lambda_i) \\ r_1 \sin(\phi + \lambda_i) = y - r_2 \sin(\lambda + \lambda_i), \end{cases} \tag{10}$$

we then see that ϕ_+ and ϕ_- can be expressed as

$$\phi_\pm = \mathrm{mod}\ (-\lambda_i + \mathrm{atan2}(y - r_2 \sin(\lambda_\pm + \lambda_i), x - r_2 \cos(\lambda_\pm + \lambda_i)), 2\pi) \tag{11}$$

where $\mathrm{atan2}(v, u)$ is the four-quadrant inverse tangent function, which gives the polar angle of point (u, v) in the x–y plane in the range $[-\pi, \pi]$. The solution (λ_+, ϕ_+) is admissible only if $\lambda_+ \in [0, \lambda_m]$ and $\phi_+ \in [0, \lambda_m]$. Similarly, the solution (λ_-, ϕ_-) is admissible only if $\lambda_- \in [0, \lambda_m]$ and $\phi_- \in [0, \lambda_m]$. If both solutions are admissible, then (x, y) belongs to two R-lines; otherwise (x, y) belongs to either one R-line or no R-line depending on whether one of the two solutions is admissible or not.

The above procedure to evaluate if a point $(x, y, h) \in \pi_h$ lies on an R-line is straightforward to implement on a computer. The result for $h = 0.2H$ was shown in figure 4(c) for a 234° T-arc. Figure 6 shows the R-line coverage for $h = 0$. In the rest of this section, we provide some geometrical insight into why these R-line coverage diagrams appear as they do.

Recall our construction of the R-line coverage in π_h as the union of translated R-arcs defined by upside cones with vertices on the upper T-arc; see figure 4. The region of R-line coverage in π_h may be geometrically understood by identifying the path traced by each extremity of the R-arcs as λ is increased from 0 to λ_m. These two paths are denoted by the dashed arcs shown in figure 7(a): the black-colored dashed arc corresponds to A_h^i, whereas the gray-colored dashed arc corresponds to the other extremity, B_h^i. Observe that any point on the path of A_h^i belongs to an R-line connecting the upper T-arc with A_-^i. Similarly, any point on the path of B_h^i belongs to an R-line connecting the upper T-arc with A_-^e. Therefore, the paths of A_h^i and B_h^i can be alternatively interpreted as the intersections of π_h with downside

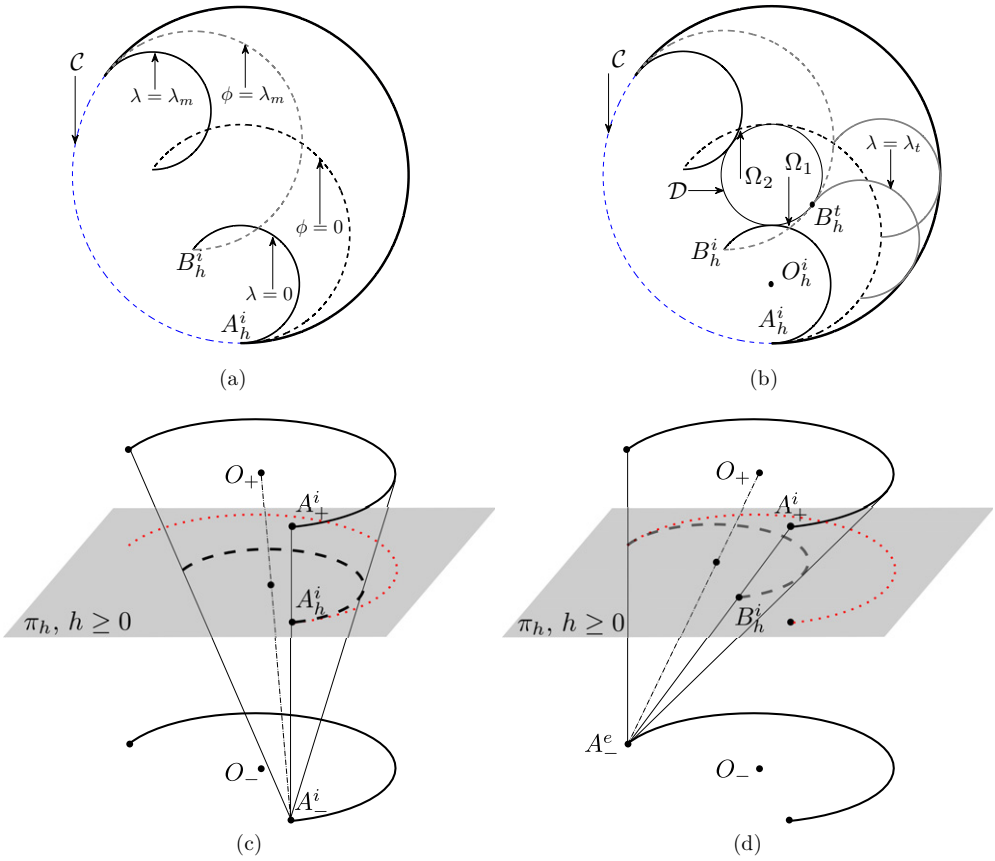

Figure 7. Arc–arc R-line coverage in π_h when the length of the T-arcs is 234°. (a) The R-arcs corresponding to $\lambda = 0$ and $\lambda = \lambda_m$ and the path traced by each extremity of these R-arcs as λ increases from 0 to λ_m. (b) The R-line coverage in π_h is characterized by five curves: the paths traced by A_h^i and B_h^i, the R-arcs at $\lambda = 0$ and $\lambda = \lambda_m$ and the circle $\mathcal{D}$. (c) The path traced by A_h^i (dashed curve), seen as the intersection of π_h with the downside cone from A_-^i. (d) The path traced by B_h^i (dashed curve), seen as the intersection of π_h with the downside cone from A_-^e.

cones from A_-^i and A_-^e; see figures 7(c) and (d). Analytically, the paths of A_h^i and B_h^i are the solutions of (4) with $\phi = 0$ and $\phi = \lambda_m$, respectively, where $\lambda \in [0, \lambda_m]$.

As illustrated in figure 7(b), the R-line coverage in π_h is fully characterized by five curves: the paths followed by A_h^i and B_h^i as λ increases from 0 to λ_m, the R-arcs corresponding to $\lambda = 0$ and $\lambda = \lambda_m$, and the circle $\mathcal{D}$ that was introduced in figure 3(b). In particular, note that the R-line coverage includes two small regions denoted as Ω_1 and Ω_2. Region Ω_1 is the area bounded by the path traced by B_h^i, the R-arc at $\lambda = 0$ and the circle $\mathcal{D}$. This region and the set of points that belong to both the convex hull of the R-arc at $\lambda = 0$ and the convex hull of the path of B_h^i are covered by the R-arcs corresponding to $\lambda \in [0, \lambda_t]$ with $\lambda_t = \lambda_m - \pi$ because these R-arcs each have two intersections with the path of B_h^i. Region Ω_2 is the mirror image of Ω_1 relative to the line that connects the midpoint of the T-arc to the center of $\mathcal{D}$; this region is created with $\lambda \in [\pi, \lambda_m]$.

The above description for the R-line coverage in π_h simplifies considerably when $h = 0$. First, the regions Ω_1 and Ω_2 disappear because $r_1 = r_2$ and thus $\mathcal{D}$ is reduced to a point. Second, the paths followed by A_h^i and B_h^i become equivalent to the R-arcs defined by upside cones with vertices A_+^i and A_+^e, respectively; this is due to the mirror symmetry relative to π_0 (i.e. the plane π_h with $h = 0$). Hence, the R-line coverage in π_0 is determined entirely by the paths followed by A_h^i and B_h^i, as shown in figure 6.

3.2. Arc–line coverage

Here, we examine the coverage associated with the R-lines that connect a point on the T-line to a point on the T-arcs. This arc–line (AL) coverage is most easily analyzed in two steps. First, we find the coverage from the T-line and the lower T-arc. Next, we find the coverage due to the T-line and the upper T-arc. The union of these two regions is the complete AL coverage.

The R-line coverage for the AL trajectory composed of the lower T-arc and the T-line is found from the following observation, which is proven in appendix B: any point P within the convex hull of the partial cone from A_+^i belongs to an R-line. Hence, the R-line coverage for this trajectory is the convex hull of the upside cone with vertex at A_+^i. See figure 8(a). This convex hull is called Λ^+.

The intersection of Λ^+ with the plane π_h characterizes the R-line coverage in π_h. This region has the form of a partial disk, as illustrated in figures 8(b) and (d) for the case $h = 0$, and can be computed with the following relations:

$$\begin{cases} (x - r_2 \cos\lambda_i)^2 + (y - r_2 \sin\lambda_i)^2 \leqslant r_1^2 \\ x \cos\alpha + y \sin\alpha \geqslant d \end{cases} \tag{12}$$

where $d = R \cos\left(\lambda_m/2\right)$ and $\alpha = (\lambda_i + \lambda_e)/2$.

The two relations in (12) may be explained as follows, using figure 9. First, the curved portion of the boundary for the partial disk in π_h is an R-arc defined by the upside cone from A_+^i. Because points on this R-arc satisfy (3) with $\lambda = 0$ and $\phi \in [0, \lambda_m]$, it follows that the curved portion of the boundary for the partial disk belongs to the circle given by the first relation in (12). Second, the straight portion of the boundary for the partial disk is determined by the line connecting A_h^i and A_h^e, which is orthogonal to the vector $\vec{m} = (\cos\alpha, \sin\alpha, 0)$ and thus yields the second relation in (12).

The R-line coverage for the AL trajectory composed of the upper T-arc and the T-line is found by symmetry: we just have to mirror the coverage for the previous AL trajectory with respect to π_0. To help visualize the situation, the upside and downside cones of R-lines resulting from mirror-symmetric AL trajectories are illustrated in figure 8(c). Hence, the sought union of R-lines is the convex hull of the downside cone from A_-^i. This convex hull is called Λ^-. The partial disk characterizing the R-line coverage in π_h for the AL trajectory composed of the upper T-arc and the T-line is defined by the relations

$$\begin{cases} (x - r_1 \cos\lambda_i)^2 + (y - r_1 \sin\lambda_i)^2 \leqslant r_2^2 \\ x \cos\alpha + y \sin\alpha \geqslant d \end{cases}. \tag{13}$$

The first inequality follows from the fact that the intersection of π_h with the downside cone from A_-^i is the arc described by (3) with $\phi = 0$ and $\lambda \in [0, \lambda_m]$. In the discussion at the end of the previous section, this arc was identified as the path followed by A_h^i. The second inequality is of course the same as in (12).

Note that the R-line coverage in π_0 is the same for both AL trajectories, due to the mirror symmetry relative to π_0. Also, for $h > 0$, the R-line coverage in π_h that comes from the T-line and the lower T-arc is always included within the coverage that comes from the T-line and the upper T-arc.

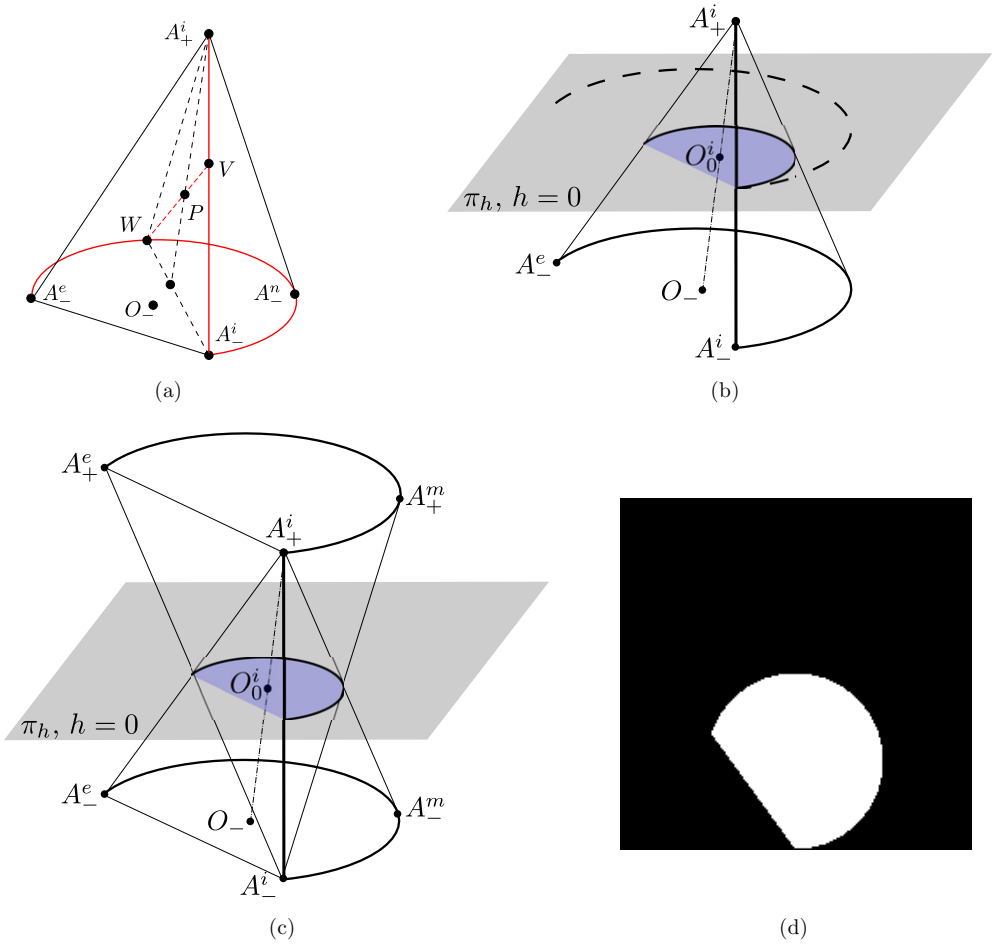

Figure 8. Arc–line R-line coverage when the length of the T-arc is 234°. The line is attached orthogonally to one of the endpoints of the T-arc. (a) Illustration for lemma 1 (b) Partial disk of R-line coverage in π_0. (c) Due to mirror symmetry with respect to π_0, the partial disk of R-line coverage in π_0 is the same for both of the AL trajectories. (d) The numerical result in π_0.

3.3. Combined coverage

Using the results of the previous sections, we can obtain the R-line coverage for the ALA trajectory. The ALA trajectory can be decomposed into three components: (i) the elemental AA trajectory consisting of the upper and lower T-arcs, (ii) the elemental AL trajectory consisting of the T-line and the lower T-arc, and (iii) the elemental AL trajectory consisting of the T-line and the upper T-arc. It follows that the union of the three sets of R-lines corresponding to these three elemental trajectories yields the complete set of R-lines for the ALA trajectory.

The ALA R-line coverage in π_h can be computed numerically by combining the procedure described in section 3.1 for the AA trajectory together with (12) and (13) for the AL trajectories. As an example, the R-line coverage in the plane $z = 0.2H$ for a 234° ALA trajectory is illustrated in figure 10. Figures 10(a) and (b) show the sets of R-line coverage for the AA

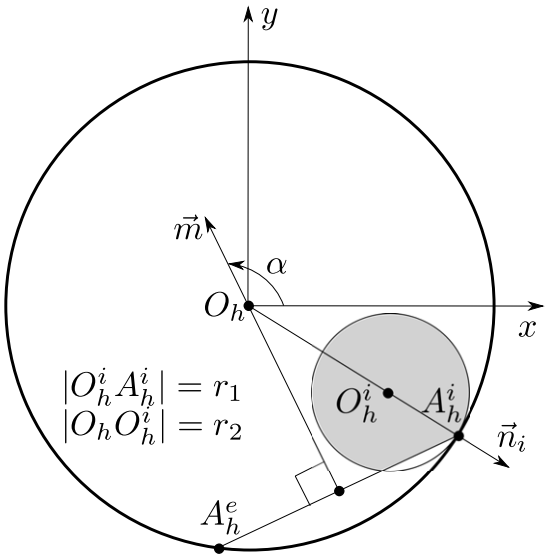

Figure 9. R-line coverage in π_h for the AL trajectory composed of the lower T-arc and the T-line.

trajectory and for the two AL trajectories, respectively, and the union of these sets is depicted in figures 10(c) and (d). From these figures, we observe that the sets of R-line coverage for the AA and AL trajectories compensate each other quite well in the plane $z = 0.2H$.

Practically, it is desirable to determine whether or not every point inside a specified ROI belongs to an R-line. The following theorem, which is proven in appendix C, and its corollary enable us to answer this question for a cylindrical ROI centered on the z-axis with radius $R_{\text{ROI}} \leqslant R_m$ and delimited by the planes $z = -H$ and $z = H$. For the statement of the theorem, we define the line $\mathcal{L}(x_0, y_0)$ to be the line parallel to the z-axis that passes through $(x_0, y_0, 0)$.

Theorem 2. *For the ALA trajectory, if* (x_0, y_0) *satisfies* $x_0^2 + y_0^2 \leqslant R_{\text{ROI}}^2$, *then there exists a coordinate* $\hat{z}$ *with* $|\hat{z}| \leqslant H$ *such that the points on the line* $\mathcal{L}(x_0, y_0)$ *that are covered by R-lines have z-coordinates in the set* $[-H, -\hat{z}] \cup [\hat{z}, H]$.

Corollary 2. *Suppose that* (x_0, y_0) *satisfies* $x_0^2 + y_0^2 \leqslant R_{\text{ROI}}^2$. *For the ALA trajectory, if a point* (x_0, y_0, z_0) *lies on an R-line, then all points* (x_0, y_0, z) *with* $z \in [-H, -|z_0|] \cup [|z_0|, H]$ *also lie on R-lines.*

Corollary 2 implies that it suffices to check the R-line coverage in the plane π_0. If the entire ROI in π_0 is covered by R-lines, then the whole ROI cylinder is also covered by R-lines.

Figures 11(a) and (b) depict the R-line coverage in the plane π_0 for ALA trajectories with angular ranges of 234° and 310°, respectively. In both figures, an ROI with radius $R_{\text{ROI}} = R\sin(27^\circ)$ is drawn (this is the largest possible ROI radius, R_m, for the 234° trajectory). Examining these figures, we observe that the R-lines do not fully cover the ROI for either of the ALA trajectories. In fact, it turns out that as long as the angular range of the ALA trajectory is less than 360°, there is always a moon-shaped region touching the origin that is not covered by R-lines. Conversely, if the angular range of the ALA trajectory is 360°, then any central ROI with $R_{\text{ROI}} \leqslant R$ is completely covered by R-lines. In the next section, we propose a modification to the ALA trajectory that addresses this problem.

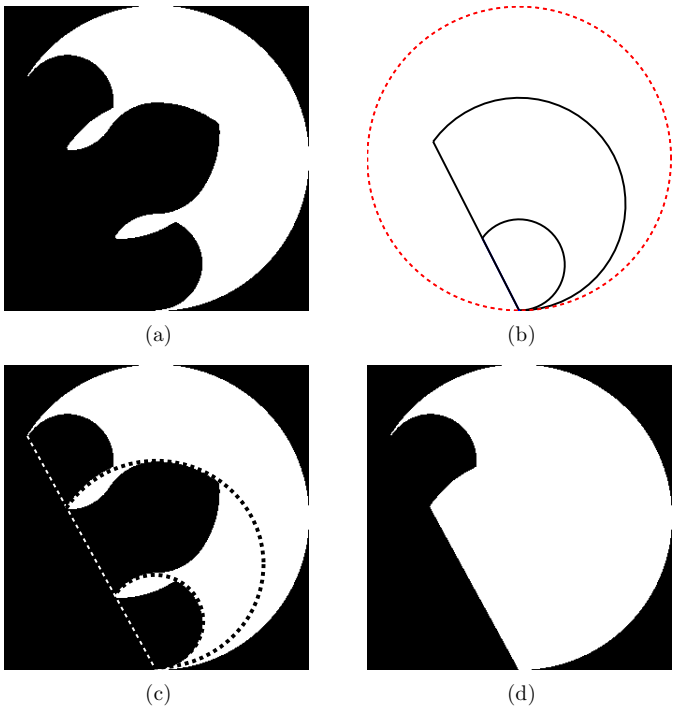

Figure 10. Combined R-line coverage resulting from arc–arc and arc–line trajectories in the plane $z = 0.2H$. (a) R-line coverage for the AA trajectory. (b) Outline of the R-line coverage for the AL trajectories; the small partial disk is for the lower T-arc and T-line, whereas the larger partial disk is for the upper T-arc and T-line. (c) Result of superimposing (b) onto (a). (d) Combined coverage.

4. The AELA trajectory

To overcome the lack of R-line coverage mentioned in the previous section, we propose the AELA trajectory, i.e the 'arc–extended-line–arc' trajectory, which was described in section 2.1. Below, we will see that the R-lines for the AELA trajectory can completely cover the ROI cylinder if the line extension is properly chosen. We will also discuss the issue of detector size and show that using the AELA trajectory for accurate CB tomography may not be constraining in terms of detector size, in comparison with performing an approximate, FDK-type, reconstruction from CB data collected on the two circular arcs only.

4.1. R-line coverage

Although theorem 2 and corollary 2 were stated for the ALA trajectory, it is important to realize that they also apply to the AELA trajectory. This is true because the proof of theorem 2 is general enough to also apply to the AELA trajectory. Therefore, corollary 2 implies that if all points inside the ROI in π_0 belong to an R-line of the AELA trajectory, then the entire ROI cylinder extending from $z = -H$ to $z = H$ is covered by R-lines. For this reason, the following arguments only focus on the R-line coverage in π_0.

As we did for the ALA trajectory, the R-line coverage for the AELA trajectory is numerically obtained by combining the results for the elemental AA and AL trajectories.

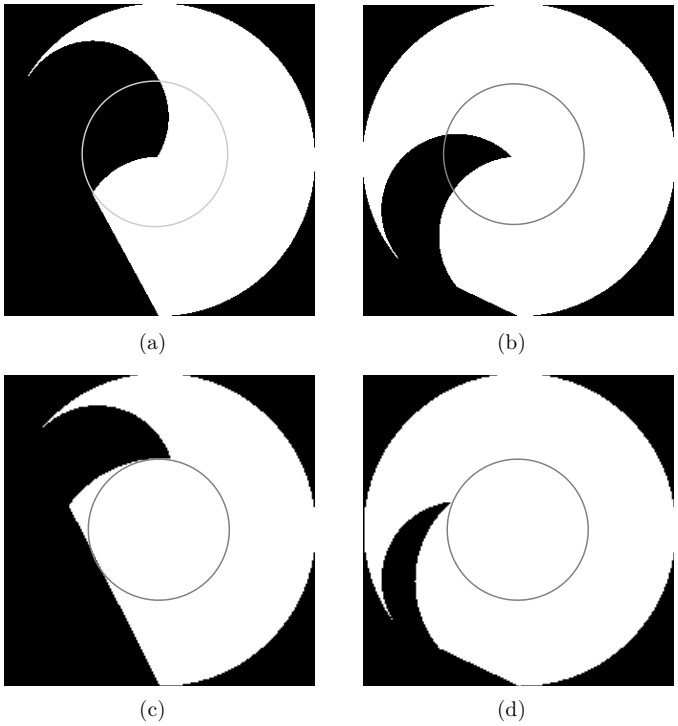

Figure 11. Numerical results for the R-line coverage in π_0 of arc–line–arc and arc–extended-line–arc trajectories. (a) Coverage of the ALA trajectory with 234° T-arcs. (b) Coverage of the ALA trajectory with 310° T-arcs. (c) Coverage of the AELA trajectory with 234° T-arcs and $\Delta h/(2H) = 0.82$. (d) Coverage of the AELA trajectory with 310° T-arcs and $\Delta h/(2H) = 0.48$.

Of course, the AA coverage remains unchanged. Only the AL coverage changes; it is now given by equations (12) and (13) upon substituting r_1' and r_2' for r_1 and r_2, respectively, with

$$r_1' = \frac{H + \Delta h - h}{2H + \Delta h} R \qquad \text{and} \qquad r_2' = R - r_1'. \tag{14}$$

Examples of the R-line coverage for the AELA trajectory in π_0 are given in figures 11(c) and (d) for source angular ranges of 234° and 310° and T-line extensions of $\Delta h/(2H) = 0.82$ and 0.48, respectively. In these figures, a circular ROI of radius $R_{\text{ROI}} = R\sin(27^\circ)$ is shown centered on the origin. Figures 11(c) and (d) demonstrate that the entire ROI is covered by R-lines when the T-line extensions are 82% and 48% of the total axial length, $2H$, when $\lambda_m = 234^\circ$ and 310°, respectively. Compared with the corresponding examples of the ALA R-line coverage depicted in figures 11(a) and (b), figures 11(c) and (d) show how the T-line extension can improve the R-line coverage.

The R-line coverage for the AELA trajectory in π_0 may be understood geometrically, as illustrated in figure 12. This figure depicts both the AA and AL contributions to the R-line coverage. From the figure, it is seen that if the T-line is extended far enough beyond the T-arcs, the partial disk of R-line coverage due to the AL elemental trajectories increases in size such that the central ROI is covered by R-lines.

An important practical question for the AELA trajectory is how large the T-line extension, Δh, needs to be so that an ROI of a given radius, R_{ROI}, is covered by R-lines. The remainder

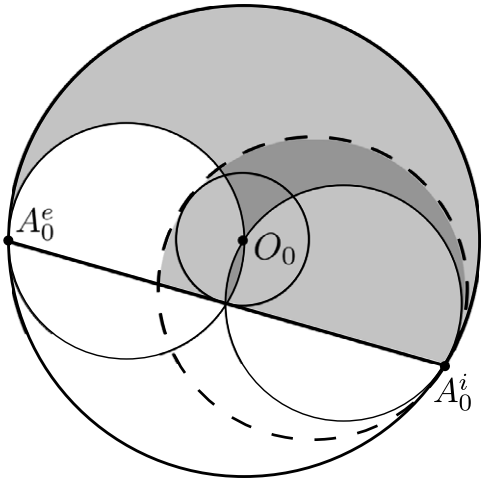

Figure 12. The R-line coverage in π_0 when the T-line of the ALA trajectory is extended beyond the T-arcs by Δh. This extension helps to increase the R-line coverage in the center. The dashed circle delineates the extra coverage resulting from the T-line extension.

of this section is devoted to answering this question. Let λ_m^* be such that the short-scan from λ_i to $\lambda_i + \lambda_m^*$ just encompasses the ROI, i.e. $\lambda_m^* = \pi + 2\arcsin(R_{\text{ROI}}/R)$. We will determine how the required Δh varies as λ_m increases from λ_m^* to 2π.

Figure 13 contains a geometrical construction depicting the R-line coverage for the AELA trajectory in π_0. In this figure, the contributions of both the AA and AL trajectories to the R-line coverage are shown in three cases: (a) $\lambda_m < \lambda_c$, (b) $\lambda_m = \lambda_c$, and $\lambda_m > \lambda_c$, where λ_c is a critical angle defined below. Observe that the R-line coverage for the AA trajectory is delimited by the T-arc, $\text{Arc}\big(O_0^i\big)$ and $\text{Arc}\big(O_0^e\big)$, and that the partial disk of R-line coverage for the AL trajectory is delimited by the dashed circle and the line $A_0^i A_0^e$. We need to calculate Δh such that the contribution of the AL trajectory to the R-line coverage includes the portion of the ROI that is not covered by the AA R-lines. This calculation requires a separation between two cases, depending on the relative position of two particular points, D and K, on the boundary of the ROI.

Let D be the point on the boundary of the ROI that is the farthest away from A_0^i. Let K be the intersection of the ROI boundary with $\text{Arc}\big(O_0^e\big)$ that is not within the triangle formed by A_0^e, A_0^i and O_0. As λ_m increases away from λ_m^*, $\text{Arc}\big(O_0^e\big)$ rotates counter-clockwise around O_0, and K moves toward D. We define λ_c to be the critical value of λ_m for which K coincides with D; see figure 13(b). Using figures 13(a) and (b), it is straightforward to see that $\lambda_c = \pi + \arccos(R_{\text{ROI}}/R)$. For $\lambda_m < \lambda_c$, K does not reach D, and the necessary Δh is independent of λ_m. To reach this conclusion, we identify all points Q that meet the following condition while being on the boundary of the ROI: any neighborhood of Q contains a subset of non-zero size that is not covered by AA R-lines. Of all such points Q, D is always the point that is the farthest away from A_0^i when $\lambda_m < \lambda_c$; thus, D consistently controls the required value for Δh, independently of λ_m. The situation changes when λ_m becomes larger than λ_c because K passes D and becomes the relevant point. As the distance from K to A_0^i decreases with λ_m, we find that the required Δh decreases with λ_m once $\lambda_m > \lambda_c$; see figure 13(c). Using these observations together with the geometrical construction of figure 13, we show in

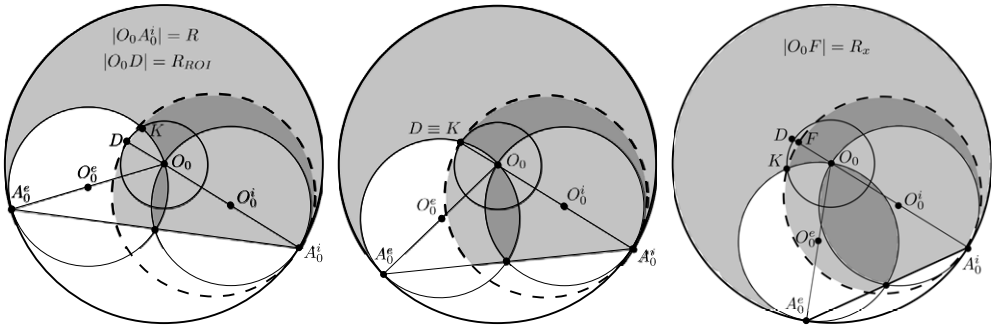

(a) $\lambda_m < \lambda_c,\ \lambda_m = \lambda_m^*$ (b) $\lambda_m = \lambda_c,\ \lambda_m > \lambda_m^*$ (c) $\lambda_m > \lambda_c,\ \lambda_m > \lambda_m^*$

Figure 13. Geometrical constructions depicting the AELA R-line coverage in π_0 for a given ROI and different values of $\lambda_m \geqslant \lambda_m^*$, where $\lambda_m^* = \pi + 2\arcsin(R_{\mathrm{ROI}}/R)$ is the minimum allowable angular length for the T-arcs, beyond which Tuy's condition is not satisfied. Two points on the boundary of the ROI play a particular role: K and D; K is the point on $\mathrm{Arc}(O_0^e)$ (i.e the R-arc from A_+^e) that is not within the triangle formed by A_0^e, A_0^i and O_0, whereas D is the point that is the farthest away from A_0^i. As illustrated in the figures, there exists a critical angle, λ_c, for λ_m where D and K become identical. The required extension for the T-line, namely Δh, takes different expressions depending on whether $\lambda_m < \lambda_c$ or not.

appendix D that the minimum relative length of the T-line extension required to cover an ROI of radius R_{ROI} with R-lines is

$$\frac{\Delta h}{2H} = \begin{cases} R_{\mathrm{ROI}}/(R - R_{\mathrm{ROI}}), & \lambda_m^* \leqslant \lambda_m \leqslant \lambda_c \\ R_x/(R - R_x), & \lambda_c < \lambda_m \leqslant 2\pi, \end{cases} \tag{15}$$

where

$$R_x = |O_0F| = d/\cos\gamma - R, \tag{16}$$

with

$$d = \sqrt{R^2 + R_{\mathrm{ROI}}^2 - 2RR_{\mathrm{ROI}}\cos\eta}, \tag{17}$$

$$\eta = \lambda_m - \arccos(R_{\mathrm{ROI}}/R), \tag{18}$$

$$\gamma = -\arcsin((R_{\mathrm{ROI}}\sin\eta)/d). \tag{19}$$

Figure 14 plots the required $\Delta h/2H$ as a function of λ_m for $R_{\mathrm{ROI}}/R = 0.15, 0.30$, and 0.45. The ratios $R_{\mathrm{ROI}}/R = 0.15$ and 0.45 are representative of current C-arm and CT scanners, respectively. Not surprisingly, figure 14 shows that the required T-line extension increases as the relative size of the ROI grows. In addition, as λ_m increases to 360°, the required Δh converges to zero, which is consistent with our findings for the full scan ALA trajectory in section 3.3.

Equation (15) can be inverted to find how $\Delta h/2H$ varies with R_{ROI}/R at fixed λ_m. Figure 15 shows this behavior for $\lambda_m = 220^\circ, 270^\circ, 310^\circ$ and 340°; as expected, the required T-line extension increases with increasing ROI size and decreases with increasing λ_m.

The plots in figures 14 and 15 indicate that the required T-line extension for the AELA trajectory is reasonable for the R_{ROI}/R ratios that are typical of current C-arm scanners (roughly 0.15). On the other hand, for larger ratios, such as those needed in CT, Δh can be fairly large when $\lambda_m = \lambda_m^*$. Fortunately, the required Δh may be reduced to any practical length by employing a suitable, larger value for λ_m.

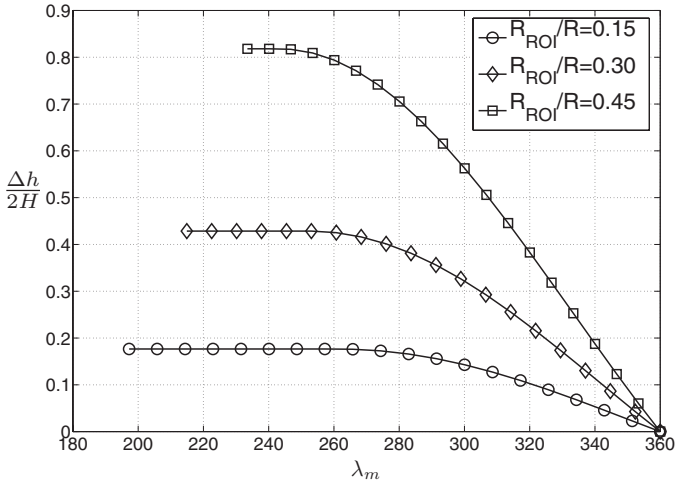

Figure 14. Minimum $\Delta h/(2H)$ required to fully cover the ROI with R-lines, plotted versus λ_m for $R_{\mathrm{ROI}}/R = 0.15$, 0.30, and 0.45.

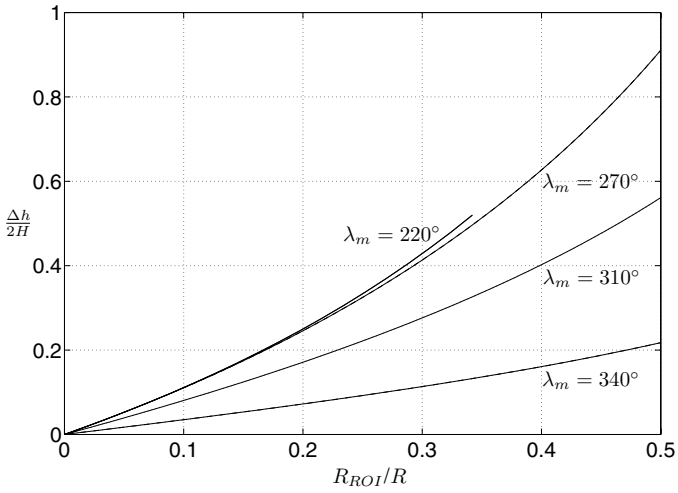

Figure 15. Minimum $\Delta h/(2H)$ required to fully cover the ROI with R-lines, plotted versus R_{ROI}/R for $\lambda_m = 220^\circ$, 270°, 310°, and 340°.

4.2. Detector size requirement

From the viewpoint of required detector size, the AELA trajectory may not look attractive at first glance. Indeed, it seems like the detector size needed for the source positions that are at the extremities, E^+ and E^-, of the extended line might be large, because these source positions must provide measurements along lines that pass through the plane $z = 0$ while $\Delta h/(2H)$ is not negligible. Fortunately, the source positions at E^+ and E^- are not needed to perform reconstruction everywhere within the ROI; they are only needed to perform reconstruction where R-line coverage of the ALA trajectory is deficient. As discussed hereafter, this aspect of the problem strongly reduces the constraint on the detector size.

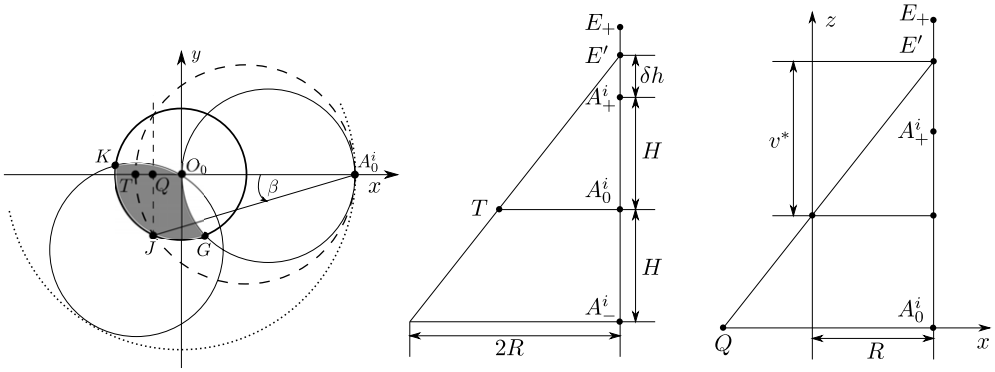

Figure 16. Detector size requirement for the AELA trajectory. Each source position E' above A_+^i allows a portion of the region that is not covered by R-lines in π_0 to be covered. This portion is the intersection of the dashed circle within the shaded area. From the viewpoint of detector size, the measurements must at least be made on the lines that connect E' to the points on this intersection. For a conventional detector arrangement, where the detector is parallel to the tangent to the T-arc and to the z-axis, this requirement implies that the detector must be large enough to cover the line connecting E' to Q.

A large variety of reconstruction algorithms may be designed for CB tomography using the AELA trajectory, some requiring more data than others. Finding the algorithm that is optimal in terms of detector size is largely outside the scope of this paper. However, a minimum requirement can be easily evaluated, namely the detector size needed to ensure that all R-lines with endpoints on the extended portion of the line are measured. This evaluation can be performed analytically using figure 16, which is drawn (without loss of generality) for the particular case where A_+^i is on the x-axis. For this evaluation, we consider a virtual detector arrangement, such that the detector contains the z-axis and is parallel to the tangent to the T-arc at A_+^i. Also, the detector rows are indexed by a Cartesian coordinate v that is equal to zero in the plane orthogonal to the z-axis through E'. The direction for v is chosen so that the rows below E' have a positive v-coordinate.

The shaded area in figure 16(a) represents the region of π_0 where there is missing R-line coverage for the ALA trajectory. Each source position E' that is above A_+^i on the extended line adds R-line coverage on a circle that intersects this shaded area, namely the dashed circle in figure 16(a). Note that this circle corresponds to the AL R-line coverage in π_0 due to E'. The portion of the dashed circle within the shaded area defines R-lines that must be measured when the source position is at E'; this portion reduces to point G when E' approaches A_+^i and to point K when E' approaches E^+. Let the point J be the intersection of the dashed circle with the ROI boundary, and let ψ be the polar angle of J. Since J lies between K and G on the ROI boundary, ψ must be between $\psi_1 = \lambda_m - \arccos(\rho)$ and $\psi_2 = 2\pi - \arccos(\rho)$ with $\rho = R_{\mathrm{ROI}}/R$. It turns out that there is a one-to-one relation between ψ and the distance δh that separates E' from A_+^i. Trigonometric calculations may be used to show that this relation is

$$\delta h = 2H\,\frac{\eta - 1}{2 - \eta} \tag{20}$$

with

$$\eta = \frac{1 + \rho^2 - 2\rho\cos\psi}{1 - \rho\,\cos\psi}\,, \tag{21}$$

where $R\,\eta$ represents the distance from A_0^i to T in figure 16(a).

Of all R-lines that must be measured with the source position at E', the line going through point J has the largest coordinate v, and this coordinate, denoted v^*, is the same as that for the line that connects E' to the orthogonal projection of J onto the x-axis, i.e. point Q in figure 16. Trigonometric calculations yield

$$\frac{v^*}{H} = \frac{1 + \rho^2 - 2\rho\cos\psi}{(1-\rho^2)\,(1-\rho\,\cos\psi)}\,, \tag{22}$$

and an analytical evaluation of this expression shows that its maximum value, v_m, over $\psi \in [\psi_1, \psi_2]$ is such that

$$\frac{v_m}{H} \leqslant 1/(1-\rho)\,. \tag{23}$$

Now, it can be shown that the detector size needed to perform an FDK-type reconstruction over the region $z \in [0, H]$ using the CB data on the upper T-arc is precisely equal to $1/(1-\rho)$. Therefore, the minimum requirement of measuring the R-lines corresponding to the extended line does not impose any extra constraint on the detector size.

5. Conclusions and discussion

We presented a thorough analysis of the R-line coverage for the arc–line–arc (ALA) trajectory. A key component of our analysis was a decomposition of the ALA trajectory into the elemental arc–arc (AA) and arc–line (AL) trajectories. For the AA trajectory, we showed that the R-line coverage in π_h can be simply described by two angles: λ and ϕ; see (3). In section 3.1, this parameterization was used to develop a procedure that enables efficient numerical evaluation of the R-line coverage for the AA trajectory. For the AL trajectory, we found that the volume of R-lines is the convex hull of a partial cone, and that the region of R-line coverage in π_h is described by either (12) or (13), depending on the orientation of the AL trajectory.

Our investigation of the R-line coverage for the ALA trajectory showed that the regions of R-line coverage for the AA and AL elemental trajectories largely complement each other. However, we found that as long as the angular length of the T-arcs is less than 360°, there is always a portion of the central ROI in π_0 that is not fully covered by R-lines. The plane π_0 is particularly important, since corollary 2 implies that when the entire ROI in this plane is covered by R-lines, the whole ROI cylinder is also covered by R-lines.

Next, to address the weakness in the R-line coverage of the ALA trajectory, we introduced the arc–extended-line–arc (AELA) trajectory, which extends the T-line beyond the T-arcs by a length Δh. Building on our analysis of the AA and AL elemental trajectories, we found that if the T-line extension is long enough, then the AELA R-lines can completely cover a central ROI. This finding was supported by a formula that may be used to calculate the necessary Δh given the ROI radius, R_{ROI}, and the angular length of the T-arcs, λ_m; see (16)–(19). Plots of $\Delta h/(2H)$ versus both λ_m and R_{ROI}/R indicated that the required T-line extension is reasonable for typical C-arm scanners.

Knowledge of the R-line coverage provided by the AELA trajectory and of the existing redundancies in this coverage enables the development of a wide variety of image reconstruction algorithms, which may be of filtered-backprojection type or not. Finding the algorithm that is the least constraining in terms of detector size was outside the scope of this paper, but definitely represents an important problem to solve, which will be part of our future investigations. However, an early study on detector size requirement was feasible. This study, presented in section 4.2, showed that the R-lines added by the line extension can be measured

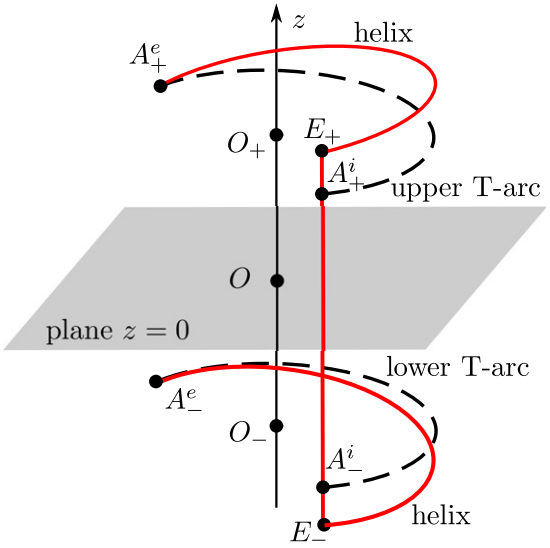

Figure 17. The helix–extended-line–helix trajectory composed of two helical segments and a line (shown with solid curves). For comparison, the arc–extended-line–arc trajectory is also illustrated with dashed curves.

with no increase in detector size, in comparison with the detector needs for performing an FDK-type reconstruction based only on the CB data from the circular arcs. Combination of this result with those published by Zamyatin *et al* (2008) provides confidence that CB tomography based on the AELA trajectory should be feasible with little extra requirement on the detector size, if any. Aside from the detector size, robustness to imperfections in the measurement geometry and to deviations from the line integral model (related, e.g., to the beam hardening effect and scattered radiation) should also be carefully considered when designing the reconstruction algorithm.

From a practical viewpoint, the T-line extension of the AELA trajectory is only moderately satisfactory because it requires a short pause in exposure. One way to circumvent this problem is to replace the two T-arcs by helical arcs that touch the extended line at its endpoints as shown in figure 17; we call this trajectory the helix–extended-line–helix (HELH) trajectory. We have performed preliminary numerical simulations with the HELH trajectory and have observed that it essentially retains the geometrical properties of the AELA trajectory studied in this work, while not requiring a pause in exposure. However, our theoretical findings for the AELA trajectory do not immediately apply to the HELH trajectory. Generalization of our theoretical results to other trajectories, such as the HELH, is an interesting topic for future research.

Acknowledgments

This work was partially supported by a grant from Siemens AG, Healthcare Sector and by the US National Institutes of Health (NIH) under grant R21 EB009168. The concepts presented in this paper are based on research and are not commercially available. Its contents are solely the responsibility of the authors and do not necessarily represent the official views of the NIH.

Appendix A

This appendix gives a proof of theorem 1, which was stated in section 2.2. To prove the theorem, we will need the following lemma. Because this is trivial, we will omit the proof.

Lemma 1. *Let π_1 and π_2 be two parallel planes, and let π_3 be another plane that is not parallel to π_1. Then the intersection between π_3 and π_1 is parallel to the intersection between π_3 and π_2.*

Now we prove theorem 1. As illustrated in figure 2(a), the intersecting plane is denoted as π_h, the vertex of the partial cone as A, and the center of the base arc as O_b. Furthermore, let B and C be the endpoints of the base arc, and let O_b' be the point where π_h intersects the line from A to O_b.

From basics of Euclidean geometry, we know that the intersection between π_h and the partial cone is an arc (which may be either circular or elliptical). This arc is denoted as $\mathrm{Arc}(O_b')$. Also, any arbitrary point, D, on the base arc can be mapped to a unique point, F', on $\mathrm{Arc}(O_b')$, and vice versa. Point F' is simply found as the intersection between π_h and the line from A to D. Again, see figure 2(a).

By construction, points A, F', D, O_b and O_b' are coplanar and define a plane Π, whose intersections with the plane of the base arc and π_h are the lines O_bD and $O_b'F'$, respectively. By lemma 1, the line O_bD is parallel to the line $O_b'F'$, i.e.

$$O_bD \| O_b'F'. \tag{A.1}$$

Therefore, the triangle AO_bD is similar to the triangle $AO_b'F'$, and hence,

$$\frac{|O_b'F'|}{|O_bD|} = \frac{|AO_b'|}{|AO_b|}. \tag{A.2}$$

Now, we isotropically scale the base arc by a scaling factor $|AO_b'|/|AO_b|$ relative to its center, O_b, to obtain the arc connecting the points G, F and E, with the scaling mapping the points B, D and C to the points G, F and E, respectively. Hence, the point F lies on the line O_bD, and (A.1) yields the relation $O_bF \| O_b'F'$. Since, by definition, $|O_bF| = |O_bD| \cdot |AO_b'|/|AO_b|$, we also have $|O_bF| = |O_b'F'|$ from (A.2). Consequently, $\overrightarrow{O_bF} = \overrightarrow{O_b'F'}$, which implies that $\overrightarrow{FF'} = \overrightarrow{O_bO_b'}$. Recall that D was chosen arbitrarily. Therefore, any point on $\mathrm{Arc}(O_b')$ can be obtained as a translation of a point on the arc connecting G, F and E by the vector $\overrightarrow{O_bO_b'}$. Because the arc connecting G, F and E is a scaled copy of the base arc, with the scaling being isotropically applied relative to O_b, the theorem is proven.

Appendix B

This appendix proves the statement made in section 3.2 that any point within the convex hull of the partial cone from A_i^+ belongs to an R-line. This proof uses figure 8(a). Let P be an arbitrary point within the convex hull, Λ^+, of the partial cone from A_+^i. Points A_+^i, A_-^i and P define a plane ζ that intersects the lower T-arc at the point W. Thus, the triangle defined by points A_+^i, A_-^i and W is the intersection between Λ^+ and ζ, and this triangle contains P. Consequently, the line through W and P must intersect the line connecting A_+^i to A_-^i at some point V which is between points A_+^i and A_-^i. Since the points V and W both belong to the source trajectory, P lies on an R-line, and the lemma is proven.

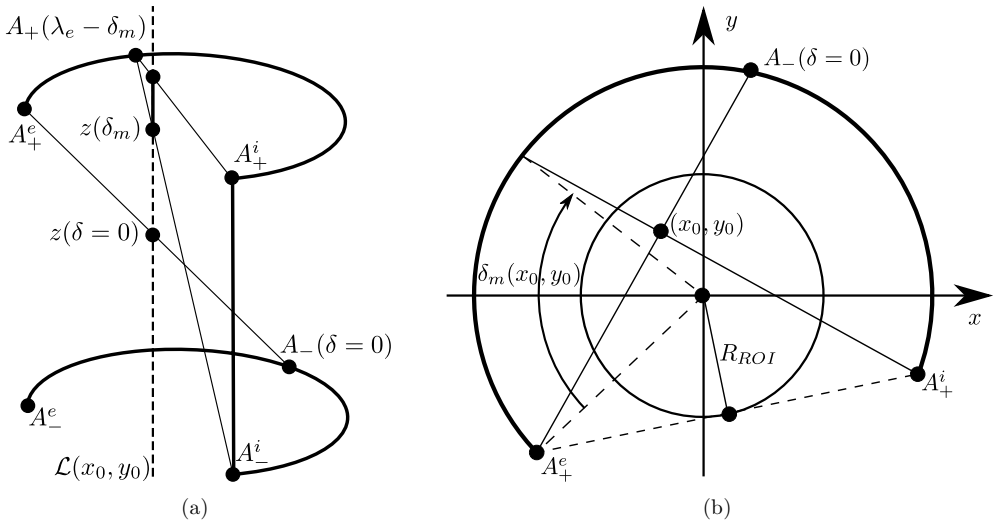

Figure C1. Diagrams used in the proof of theorem 2. (a) The ALA trajectory. (b) Orthogonal projection of the ALA trajectory onto π_0.

Appendix C

This appendix provides a proof of theorem 2, which was stated in section 3.3. For this proof, refer to figure C1. Consider an arbitrary pair of x–y coordinates, (x_0, y_0), such that $x_0^2 + y_0^2 \leqslant R_m^2$, and let $\mathcal{L}(x_0, y_0)$ be the line parallel to the z-axis through $(x_0, y_0, 0)$. We define a function $z(\delta)$ as follows. First, let $A_+(\lambda_e - \delta)$ be the point at polar angle $\lambda_e - \delta$ on the upper T-arc, and let Π be the plane defined by $A_+(\lambda_e - \delta)$ and $\mathcal{L}(x_0, y_0)$. Second, let the point $A_-(\delta)$ be the intersection of Π with the lower T-arc. Denote the R-line connecting $A_+(\lambda_e - \delta)$ and $A_-(\delta)$ as L. Because L and $\mathcal{L}(x_0, y_0)$ are coplanar and not parallel, they have an intersection at some point $(x_0, y_0, z(\delta))$.

As δ increases from zero, $A_-(\delta)$ moves toward A_-^i, so that $z(\delta)$ is a well-defined function only for $\delta \in [0, \delta_m]$, where δ_m is such that $A_-(\delta_m)$ is the same point as A_-^i. Note that $(x_0, y_0, z(\delta_m))$ is thus the intersection of $\mathcal{L}(x_0, y_0)$ with the R-line connecting A_-^i and $A_+(\lambda_e - \delta_m))$. Because the upper and lower T-arcs are connected curves, the function $z(\delta)$ is continuous.

Let $\hat{z} = \min_{\delta \in [0, \delta_m]} z(\delta)$. It follows that all points (x_0, y_0, z) with $z \in [\hat{z}, z(\delta_m)]$ are covered by R-lines with endpoints on the upper T-arc and the lower T-arc. Now, observe that all points (x_0, y_0, z) with $z \in [z(\delta_m), H]$ are covered by R-lines with endpoints on the upper T-arc and the portion of the T-line that is between the two T-arcs, the endpoint on the upper T-arc being always $A_+(\lambda_e - \delta_m)$. Therefore, all points (x_0, y_0, z) with $z \in [\hat{z}, H]$ are covered by R-lines. By the symmetry of the ALA trajectory, all points (x_0, y_0, z) with $z \in [-\hat{z}, -H]$ are also covered by R-lines.

Appendix D

In this appendix, we derive the result expressed by (15)–(19) for the minimum T-line extension, Δh, needed to guarantee that the AELA trajectory covers the ROI with R-lines.

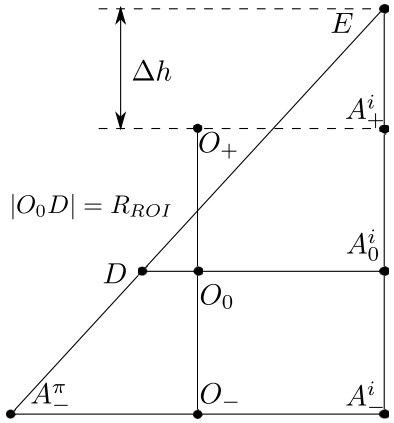

Figure D1. Axial cross section of the AELA trajectory in the plane Π used in appendix D.

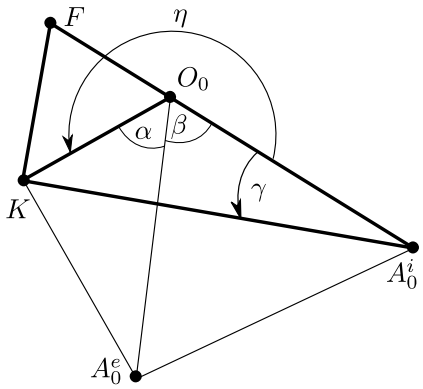

Figure D2. Triangle extracted from figure 13(c) to derive the formula for $R_x = |O_0F|$.

We start by proving (15) for the case $\lambda^*_m \leqslant \lambda_m \leqslant \lambda_c$; see figure 13(a). Consider the plane, Π, containing the z-axis and the point A^i_0. As depicted in figure D1, this plane contains the initial points of the T-arcs, A^i_- and A^i_+, together with the points A^i_0, O_0, and D that are shown in figure 13(a). Also, figure D1 labels the intersection of Π with the lower T-arc as A^π_- and the upper endpoint of the extended T-line as E. Since the triangle $A^\pi_- E A^i_-$ is similar to the triangle DEA^i_0, we have

$$\frac{\left|A^i_- E\right|}{\left|A^\pi_- A^i_-\right|} = \frac{\left|A^i_0 E\right|}{\left|DA^i_0\right|}, \tag{D.1}$$

which simplifies to

$$\frac{2H + \Delta h}{2R} = \frac{H + \Delta h}{R_{\mathrm{ROI}} + R}. \tag{D.2}$$

Some algebra then yields

$$\frac{\Delta h}{2H} = \frac{R_{\mathrm{ROI}}}{R - R_{\mathrm{ROI}}}, \tag{D.3}$$

which is the desired equation. The second case in (15) for $\lambda_c \leqslant \lambda_m \leqslant 2\pi$ is proven similarly, with D replaced by F in figure D1.

Next, we derive (16)–(19), which describe $R_x = |O_0F|$. For this derivation, see figure D2, which refers to several points in figure 13(c) and also labels the angles α, β, γ, and η. First, note that $R_x = \left|A_0^iF\right| - \left|A_0^iO_0\right| = \left|A_0^iF\right| - R$. Substituting the relation $\left|A_0^iF\right| = \left|A_0^iK\right|/\cos\gamma$ and defining $d = \left|A_0^iK\right|$, we obtain

$$R_x = d/\cos\gamma - R. \tag{D.4}$$

By the law of cosines,

$$\left|A_0^iK\right|^2 = |O_0K|^2 + \left|A_0^iO_0\right|^2 - 2|O_0K|\left|A_0^iO_0\right|\cos(\alpha+\beta). \tag{D.5}$$

Recalling that $d = \left|A_0^iK\right|$, $|O_0K| = R_{\mathrm{ROI}}$, and $\left|A_0^iO_0\right| = R$, and using the fact that $\eta = 2\pi - (\alpha+\beta)$, (D.5) yields

$$d = \sqrt{R_{\mathrm{ROI}}^2 + R^2 - 2RR_{\mathrm{ROI}}\cos\eta}. \tag{D.6}$$

Observe that $\alpha = \arccos(R_{\mathrm{ROI}}/R)$ and $\beta = 2\pi - \lambda_m$. So η may be expressed as

$$\eta = \lambda_m - \arccos(R_{\mathrm{ROI}}/R). \tag{D.7}$$

Finally, application of the law of sines gives $|O_0K|/\sin\gamma = \left|A_0^iK\right|/\sin(\alpha+\beta)$, which implies $\sin\gamma = -(R_{\mathrm{ROI}}\sin\eta)/d$. Hence,

$$\gamma = -\arcsin((R_{\mathrm{ROI}}\sin\eta)/d). \tag{D.8}$$

References

Cho S, Xia D, Pellizzari C A and Pan X 2008 Exact reconstruction of volumetric images in reverse helical cone-beam CT *Med. Phys.* **35** 3030–40

Cho S, Xia D, Pellizzari C A and Pan X 2010 A BPF-FBP tandom algorithm for image reconstruction in reverse helical cone-beam CT *Med. Phys* **37** 32–9

Finch D V 1985 Cone beam reconstruction with sources on a curve *SIAM J. Appl. Math.* **45** 665–73

Hoppe S, Dennerlein F, Lauritsch G, Hornegger J and Noo F 2006 Cone-beam tomography from short-scan circle-plus-arc data measured on a C-arm system *IEEE Nuclear Science Symp. Conf. Record* pp 2873–7

Katsevich A 2004a Image reconstruction for the circle and line trajectory *Phys. Med. Biol.* **49** 5059–72

Katsevich A 2004b An improved exact filtered backprojection algorithm for spiral computed tomography *Adv. Appl. Math* **32** 681–97

Katsevich A 2005 Image reconstruction for the circle-and-arc trajectory *Phys. Med. Biol.* **50** 2249–65

Noo F, Wunderlich A, Lauritsch G and Kudo H 2009 On the problem of axial data truncation in the reverse helix geometry *10th Int. Meeting on Fully Three-Dimensional Image Reconstruction in Radiology and Nuclear Medicine* pp 90–3

Pack J D and Noo F 2005 Cone-beam reconstruction using 1D filtering along the projection of M-lines *Inverse Problems* **21** 1105–20

Pack J D, Noo F and Clackdoyle R 2005 Cone-beam reconstruction using the backprojection of locally filtered projections *IEEE Trans. Med. Imaging* **24** 70–85

Tuy H K 1983 An inversion formula for cone-beam reconstruction *SIAM J. Appl. Math.* **43** 546–52

Ye Y, Zhao S, Yu H and Wang G 2005 A general exact reconstruction for cone-beam CT via backprojection-filtration *IEEE Trans. Med. Imaging* **24** 1190–8

Zamyatin A, Katsevich A and Chiang B S 2008 Exact image reconstruction for a circle and line trajectory with a gantry tilt *Phys. Med. Biol.* **53** N423–35

Zou Y and Pan X 2004 Exact image reconstruction on pi-lines from minimum data in helical cone-beam CT *Phys. Med. Biol.* **49** 941–59